Strongly out-of-equilibrium growth morphologies in fast solidifying eutectics

G. Boussinot,[1,*] M. Döring,[2,3] M. Schmidt,[2,3] and M. Apel[1]

[1]*Access e.V., Intzestr. 5, 52072 Aachen, Germany*

[2]*Institut of Photonic Technologies (LPT), Friedrich-Alexander UniversitŁt Erlangen-Nrenberg, Konrad-Zuse-Str.3-5, 91052 Erlangen, Germany*

[3]*Erlangen Graduate School in Advanced Optical Technologies (SAOT), Paul-Gordan-Strasse 6, 91052 Erlangen, Germany*

(Received 26 May 2021; revised 7 March 2022; accepted 13 April 2022; published 25 April 2022)

In metal printing processes such as laser-based additive manufacturing, typical solidification velocities yield a strongly out-of-equilibrium (SOE) growth regime that is intermediate between the slow solidification in conventional metal casting and rapid solidification regimes characterized by severe solute trapping. Using phase-field simulations supported by experimental observations, we provide evidence for an inherent growth mode of the SOE regime in slightly hypereutectic Al-Ni, leading to the destabilization of the planar eutectic coupled growth front and the development of a protruded state. We interpret this scenario theoretically in terms of a concomitant growth of different solidification modes, here the coupled eutectic together with α primary phase. As another example of concomitant growth under SOE conditions, we present simulation results for single-phase solidification of a Ni fcc-phase exhibiting dendrites and doublons.

DOI: 10.1103/PhysRevMaterials.6.043405

I. INTRODUCTION

The solidification of a pure substance or of an alloy has been the subject of an enormous body of studies in the literature, of course owing to the practical interest of metallurgical processes, but also because it represents an archetype of nonlinear dynamics leading to pattern formation [1]. In particular, dendritic and eutectic growths have attracted a lot of attention of physicists in the 1980s and the 1990s. The dendritic theory, based on the pioneering work by Ivantsov [2], was developed in order to account for the uniqueness of the operating state observed in the experiments. The selection mechanism, providing the relation between growth velocity and undercooling, turned out to be subtly related to the anisotropy of surface tension [3–6]. In opposition, a so-called parity-broken dendrite or doublon was found in the absence of anisotropy [7,8].

Eutectic coupled growth was also extensively studied. First, its basic state was described in the seminal paper by Jackson and Hunt (JH) [9]: for a given growth velocity V, the temperature of the growth front depends on the periodicity λ of the lamellar or fibrous structure. Steady states were found within a continuous interval of λ [10,11], and several branches were found [12], showing oscillatory, tilted, or indented structures [13–15]. In general, a large variety of growth patterns were evidenced, illustrating bifurcations, symmetry breaking, or period doubling as fundamental concepts of nonlinear dynamics. It should be noted that hybrid objects exhibiting a fine eutectic structure and a dendritic shape on a larger scale were also evidenced [16–18].

While the predominance of boundary-integral techniques [3,4,7,12,14] had restricted the studies to two dimensions, the phase field method enabled scientists to tackle three-dimensional problems. In particular, the three-dimensional dendritic theory [6] was confirmed by Karma and Rappel [19]. More recently, large arrays of dendrites under directional solidification conditions were simulated [20]. On the side of eutectics, the lamellae-to-rod transition [21], the zigzag bifurcation [22], or the spiral dendrite [23], could be investigated. In opposition to the boundary-integral technique, phase field models are nowadays also able to treat the problem of a contrast of diffusivity between the growing and the mother phase [24], owing to the introduction of a kinetic cross coupling [25].

Recently, the development of laser-based additive manufacturing has lead to a renewed attention on solidification at larger velocities. In contrast to highly undercooled levitated droplets [26,27], here the laser scanning speed provides an upper bound for the solidification velocity and clearly the latter remains well below the absolute stability velocity, corresponding to rapid solidification, for which pattern formation is highly suppressed and flat front solidification takes place [28]. In Ref. [29], some of us investigated, using phase field simulations and experiments, the columnar solidification that takes place in laser powder bed fusion (LPBF) experiments. Using theoretical arguments inherited from the dendritic theory, the commonly observed cellularlike growth directed along the cubic axis of the underlying crystal was explained in terms of the strongly out-of-equilibrium (SOE) regime. The latter is defined through the dimensionless driving force Δ, and is intermediate between the weakly out-of-equilibrium regime for which $\Delta \ll 1$ and the regime approaching rapid solidification for which $1-\Delta \ll 1$. In the SOE regime Δ and $1-\Delta$ are of the same order. Then, the growth front temperature T_i is neither close to the liquidus temperature T_L nor close to the solidus temperature T_S for the single-phase SOE solidification studied in Ref. [29], for which $\Delta = (T_i - T_L)/(T_S - T_L)$.

*g.boussinot@access-technology.de

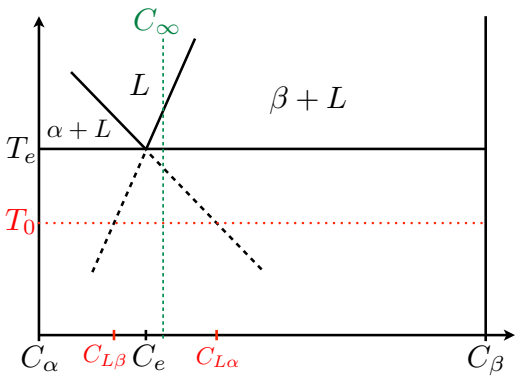

FIG. 1. Schematic phase diagram focused on the eutectic plateau of the Al-Ni binary system. The concentration in the α and the β phases are approximately independent of temperature, and the difference in liquidus concentrations $C_{L\alpha}$ and $C_{L\beta}$ defines the driving force Δ_L when the front temperature T_0 deviates from the eutectic temperature T_e (see text). C_∞ is the global concentration of the alloy that is reached far ahead of the solidification front through diffusion of solute.

In the present article we evidence using three-dimensional phase field simulations, a scenario leading to a destabilization of the eutectic coupled growth in a slightly hypereutectic Al-Ni alloy. In particular, we show that our simulations reproduce faithfully the mixed dendritic/eutectic regime that we observe experimentally. We analyze this regime and attribute its peculiarity, i.e., the concomitant growth of different solidification modes, to the SOE conditions. Finally, we give another example of such a concomitant growth with two-dimensional simulations of a single-phase solidification structure composed of dendrites and doublons.

II. STRONGLY OUT-OF-EQUILIBRIUM REGIME IN THE Al-Ni EUTECTIC SYSTEM

A. Phenomenology of eutectic coupled growth

The Al-Ni binary system presents a eutectic temperature (see Fig. 1) below which the liquid L loses stability to the benefit of the α phase, almost pure in aluminum, and the intermetallic β phase Al_3Ni. Owing to the fact that the eutectic concentration C_e is small, i.e., around 6 wt. % Ni (compared to 42 wt. % Ni in β), the coupled growth takes place through thin fibers of β phase embedded in a matrix of α phase [30,31]. At low velocities, coupled growth occurs when the alloy concentration is in the neighborhood of the eutectic concentration, while dendrites of α (β) phase grow when the deviation from eutectic concentration is large enough on the hypo(hyper)-eutectic side. The outcome of this competition between coupled and dendritic growths provides the boundaries of the so-called coupled zone [32], in which coupled growth is dominant.

During the latter, the solute is rejected by the α phase and absorbed by the β phase. The coupled motion of the α/liquid and β/liquid interfaces is driven by concentration gradients in the liquid that may be quantified using a dimensionless driving force Δ_L. This driving force describes the deviation from eutectic temperature and is proportional to the difference in liquidus concentrations $C_{L\alpha}$ and $C_{L\beta}$, i.e.,

$$\Delta_L = \frac{C_{L\alpha} - C_{L\beta}}{C_\beta - C_\alpha}. \tag{1}$$

As we infer from Fig. 1, when the temperature of the growth front T_0 is close enough to the eutectic temperature T_e, the variations of concentration in the liquid L are small compared to the width of the eutectic plateau $C_\beta - C_\alpha$, and $\Delta_L \ll 1$. This corresponds to the weakly out-of-equilibrium (WOE) regime for which the JH theory was developed. Diffusion takes place in the liquid through concentration gradients of order Δ_L/λ, and the conservation of mass at the interfaces moving at velocity V implies

$$V \sim D\,\frac{\Delta_L}{\lambda}, \tag{2}$$

where D is the diffusion coefficient in the liquid. On the other hand, capillary effects proportional to the capillary length d_0 are present due to the curvature of the solid/liquid interfaces, and their magnitude d_0/λ is of order Δ_L, yielding the well-known scaling relation between λ and V:

$$\frac{\lambda}{d_0} \sim \left(\frac{V d_0}{D}\right)^{-1/2}. \tag{3}$$

We see that the diffusion length $l_D = D/V$ obeys $l_D \sim \lambda/\Delta_L$ and is thus much larger than the spacing λ in the WOE regime, i.e., when $\Delta_L \ll 1$. Moreover, far ahead of the growth front, the global concentration of the alloy C_∞ is reached through a gradient on the scale of the diffusion length. The magnitude of this gradient is related to the driving force for single-phase solidification (in our case the solidification of α)

$$\Delta_\alpha = \frac{C_{L\alpha} - C_\infty}{C_{L\alpha} - C_\alpha}, \tag{4}$$

and is of order Δ_α/l_D. We thus see that, in the WOE regime, this gradient becomes comparable with the gradient responsible for coupled growth Δ_L/λ when Δ_α becomes of order unity, i.e., when the deviation from C_e of the hypoeutectic concentration C_∞ is comparable to the concentration gap $C_e - C_\alpha$. The equality of these two gradients may be envisioned as a definition of the boundary of the coupled zone.

B. Destabilization of eutectic coupled growth

According to our phase field simulations and experiments [33,34], the phenomenology presented just above breaks down precisely at growth velocities that are typical for the LPBF additive process. The new phenomenology that arises is related to the shape of the coupled zone in Al-Ni. Already long ago, it was noticed that the coupled zone in Al-Ni is skewed towards hypereutectic concentrations [35]. This means that alloys increasingly rich in Ni may be solidified via coupled growth by increasing the growth rate. In Ref. [33] we have evidenced both numerically and experimentally this skewness of the coupled zone in Al-Ni. In particular, for a given 10 cm/s laser scanning speed, the area fraction of the melt pool which exhibits coupled growth increases with increasing Ni concentration in the alloy. This shows that the larger C_∞, the larger the solidification velocity at which coupled growth is possible. It was suggested that the asymmetry of the phase diagram,

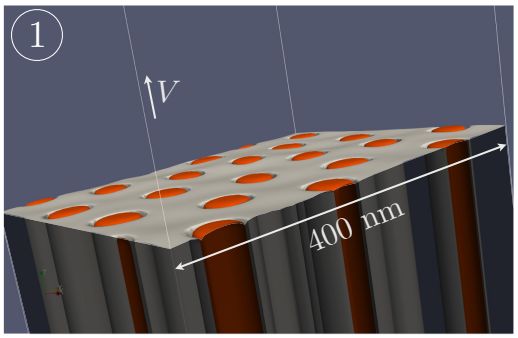

FIG. 2. Planar coupled growth pattern that we obtain for $V = 0.5$ cm/s.

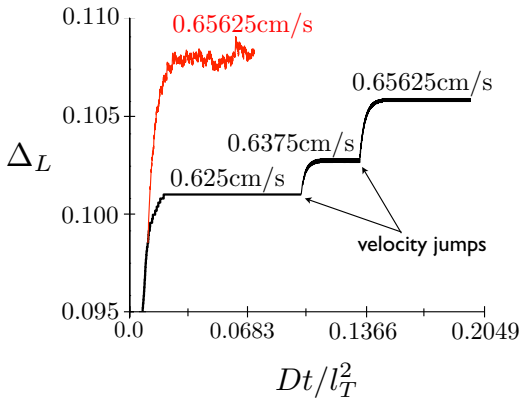

FIG. 3. Time evolution of the growth front temperature expressed by the eutectic undercooling Δ_L for the indicated velocities. The two successive velocity jumps yield a stable planar coupled growth for $V = 0.65625$ cm/s, while a chaotic dynamics may also be observed at this velocity (red curve).

i.e., the large difference between $C_\beta - C_e$ and $C_e - C_\alpha$, is responsible for an increase of the liquid concentration at the growth front when out-of-equilibrium effects become important. Then, the diffusion flux on the scale of the diffusion length that allows the diffusion field to reach C_∞ ahead of the solidification front inevitably overcomes the diffusion flux responsible for coupled growth, and α dendritic growth takes over at higher solidification velocities, as observed experimentally in the bulk of the melt pool.

Let us now investigate in detail by numerical simulations how the destabilization of coupled growth occurs. Three-dimensional phase field simulations are performed using the software MICRESS [36], in which the phase field model [37,38] is coupled to the SSOL6 (SGTE Alloy Solutions Database v6.0) thermodynamic database for the Al-Ni system. Purely isotropic solid/liquid surface tensions ($\sigma_0 = 10^{-5}$ J/cm^2) and kinetic coefficients [$\mu_0 = 10$ cm^4/(J s)] are assumed, and the local driving force (in J/cm^3) at the interface is calculated using the thermodynamic database. The mobility correction that appears in the frame of the thin-interface limit is also taken into account. The diffusion coefficient is assumed as constant and equal to 2×10^{-5} cm^2/s.

A constant and unidirectional thermal gradient $G = 10^5$ K/cm, typical for the LPBF process [39], is imposed and the growth velocity V, aligned with the thermal gradient, is varied between 0.5 and 1.5 cm/s. The initial conditions correspond to a planar solidification front at a temperature slightly below the eutectic temperature ($\Delta_L \simeq 0.02$) with four unevenly spaced fibers. In the growth direction, the diffusion field is assumed unidimensional at distances larger than 300 nm from the growth front, kept fixed in the simulation box by a moving frame procedure. Perpendicularly to the growth direction, the simulation domain represents 330 nm $\times$ 400 nm. The discretization step is 2.5 nm and periodic conditions are applied to each boundary of the simulation box whose normal vector is perpendicular to the growth direction. At the hot end of the simulation box, i.e., in the liquid far ahead of the growth front, a 9 wt. % Ni hypereutectic concentration is fixed (we recall that the eutectic concentration corresponds to 6 wt. % Ni).

For the lowest velocities, planar coupled growth, with the axis of the fibers aligned with the growth direction, is found as presented in Fig. 2 for $V = 0.5$ cm/s. This "classical" eutectic coupled growth mode is found stable for velocities $V \leqslant 0.625$ cm/s. In Fig. 3 the time evolution of the dimensionless growth front temperature Δ_L (defined as the "hottest" position of the solid), is plotted. Since in our study V varies and the thermal gradient G remains fixed, the time unit l_T^2/D is defined through the thermal length $l_T = \delta T/G$, where δT is the temperature interval corresponding to $0 < \Delta_L < 1$ (here 121 K for the Al-Ni binary alloy with a 920 K eutectic temperature). We see that for $V = 0.625$ cm/s the initial transient leads to a constant undercooling. Actually, the growth is not strictly speaking at steady state because spacing adjustment slowly takes place, but the variations in time of the undercooling are undistinguishable on the scale of Fig. 3.

In opposition, a destabilization of the planar coupled growth takes place at $V = 0.65625$ cm/s. The growth mode bifurcates towards a chaotic dynamics, corresponding to the red curve in Fig. 3 that indicates irregular front temperature variations over time. This mode corresponds to the microstructure in Fig. 4. The chaotic dynamics is sustained by so-called termination events, i.e., individual fibers disappear in the rear of the growth front. In WOE eutectic growth, this termination is known to be the process by which the planar coupled growth structure accommodates and evolves towards a stable spacing when the initial one is too small [10]. In this case, the lateral solute fluxes responsible for coupled growth

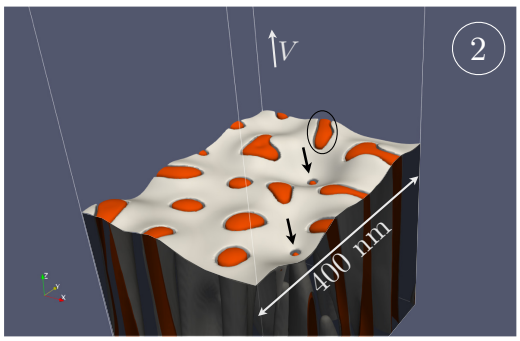

FIG. 4. Chaotic eutectic growth pattern that we obtain for $V = 0.65625$ cm/s. The arrows indicate termination events, and the encircling illustrates the elongation of the β fibers.

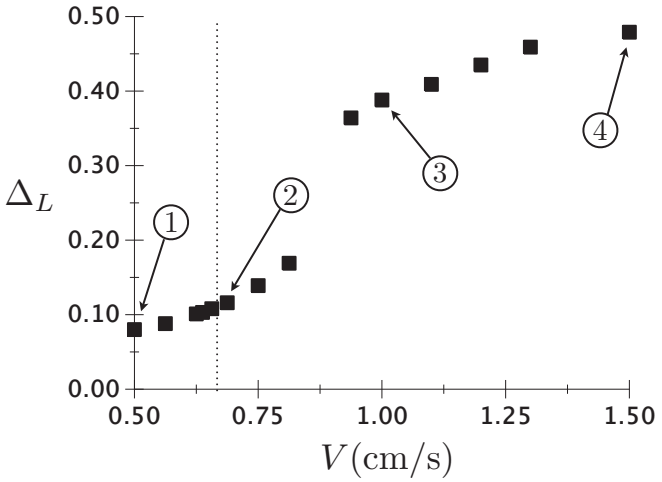

FIG. 5. Eutectic undercooling Δ_L as a function of the growth velocity V. The vertical dotted line denotes the transition, when V increases, towards a chaotic dynamics. A jump of Δ_L is observed between $V = 0.8125$ cm/s and $V = 0.9375$ cm/s, corresponding to the appearance of the protruded state and the entrance in the SOE regime. The numbering from 1 to 4 is intended to facilitate the link with Figs. 2, 4, 7, and 8.

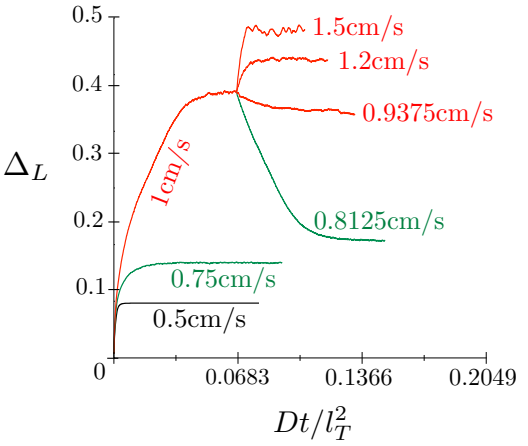

FIG. 6. Time evolution of the growth front undercooling Δ_L for the indicated velocities. In black: planar coupled growth; in green: chaotic eutectic coupled growth; in red: protruded growth.

(of order Δ_L/λ as mentioned above) are largely predominant, the termination of a fiber only produces a slight perturbation of the growth front, and the planar growth is maintained. In case of the chaotic dynamics, the termination events, indicated by the arrows in Fig. 4, produce a groove in the growth front that ceases to be planar. This allows the velocity of the β/liquid interfaces to acquire a significant component perpendicular to the growth direction, yielding an elongation of the fibers as illustrated by the encircling of one of them in Fig. 4. This dynamics seems closely related to the one leading to large amplitude oscillations in two-dimensional eutectic growth, reported experimentally [40] and using phase field simulations [41]. In the course of time, the termination events are compensated by a splitting of elongated fibers, which together leads to the chaotic dynamics as a quasistationary growth process.

As also visible in Fig. 3, when the quasi-steady-state configuration obtained for $V = 0.625$ cm/s is subjected to a jump in velocity, bringing it to $V = 0.6375$ cm/s, the planar coupled growth remains stable. Subsequently, when the velocity experiences a second jump to $V = 0.65625$ cm/s, the planar coupled growth also remains stable, although this velocity is the same as for the red curve, demonstrating bistability of the growth regime. Note also that the difference in undercooling for these two states is relatively small, the undercooling of the chaotic regime being of course quantified using an average over time.

When we plot the undercooling as a function of the velocity V in Fig. 5, the bifurcation towards chaos, represented by the vertical dotted line, is found to be rather smooth. Let us note that the two undercoolings corresponding to the bistability at $V = 0.65625$ cm/s are undistinguishable on this scale. In opposition, a discontinuity in Δ_L is observed between $V = 0.8125$ cm/s and $V = 0.9375$ cm/s. The results for these two velocities are obtained by the application of a velocity drop to the configuration at $V = 1$ cm/s. The time evolution of Δ_L as plotted in Fig. 6 shows that for $V = 1$ cm/s a long initial transient leads to a stabilization of the undercooling around $\Delta_L \simeq 0.39$. When the velocity drops to $V = 0.8125$ cm/s, the front undercooling decreases drastically to a value $\Delta_L \simeq 0.17$ that is close to the result for $V = 0.75$ cm/s, i.e., $\Delta_L \simeq 0.14$. In opposition, Δ_L remains close to 0.39 when the velocity drops to $V = 0.9375$ cm/s.

This qualitative difference corresponds to the jump in Δ_L observed in Fig. 5 and to the emergence of a new pattern that we present in Fig. 7 for $V = 1$ cm/s. A protrusion of α phase emerges and tends to grow at a slightly higher temperature than the eutectic structure. Here, again, the dynamics is chaotic. The protrusion repeatedly vanishes and reappears in another part of the simulation domain (see movie 1 in the

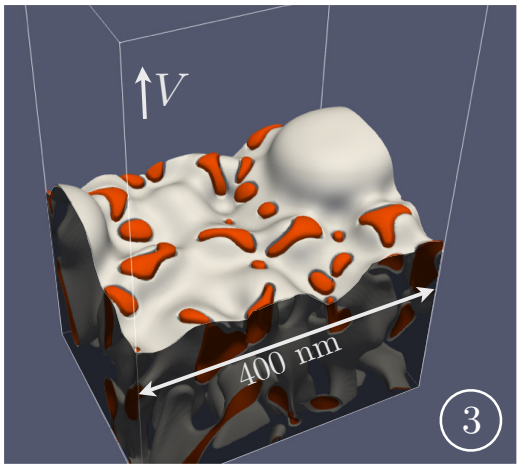

FIG. 7. Protruded state of growth for $V = 1$ cm/s. The protrusion repeatedly vanishes and reappears at a new location in the simulation domain with an associated timescale on the order D/V^2. Its extension, i.e., the difference in temperature between the protrusion's tip and the eutectic structure, is in this snapshot maximal. We refer to movie 1 in the Supplemental Material [42] for an evolution at $V = 1.1$ cm/s, very similar to $V = 1$ cm/s.

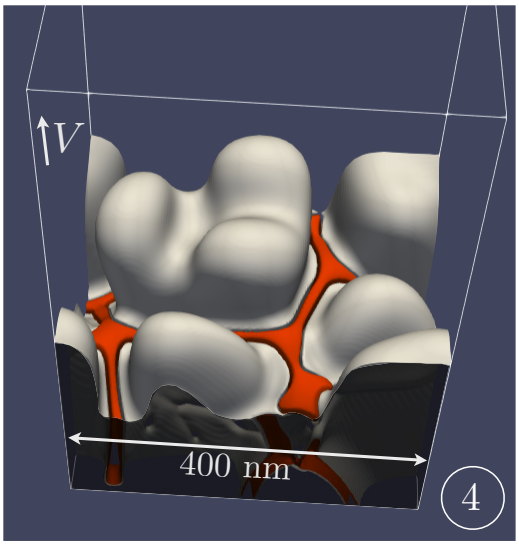

FIG. 8. Protruded state with several protrusions that we obtain for $V = 1.5$ cm/s. The extension of the protrusion is larger than for $V = 1$ cm/s, illustrating the phenomenology of the competition between coupled growth and single-phase α growth (see text).

Supplemental Material [42] for $V = 1.1$ cm/s). The snapshot that is presented in Fig. 7 represents a time at which the protrusion has its largest extension. During the lifetime of a given protrusion, a cylinder in which β fibers are absent develops in the solid in the rear of the growth front.

In Fig. 5 we see that Δ_L continues to increase with V after the jump in Δ_L, i.e., for $V > 0.9375$ cm/s. In Fig. 8 the pattern that is obtained for $V = 1.5$ cm/s is presented. Several protrusions of α phase grow at higher temperature than the β phase within the simulation domain, and this difference in growth temperature is substantially larger than for $V = 1$ cm/s. Moreover, the β phase develops interconnected lamellae instead of fibers, as a result of mass conservation and of the fact that now a large portion of the growth front is filled with protrusions. The dynamics of their tip is more complex than for $V = 1$ cm/s, at which the protrusion simply develops and then disappears. We see in Fig. 8 that for example the tip may split. The protrusions are actually in competition, with some of them vanishing and others growing, the difference in temperature between the most advanced tips and the β phase remaining mainly constant in time.

As mentioned above, the solid/liquid interfaces' properties are assumed isotropic in the simulations, while the anisotropy of the α-liquid surface tension in metallic alloys is typically on the order of a few percent, and the anisotropy of kinetic coefficient, which is less easy to apprehend, most likely presents the same order of magnitude. Thus, in view of the importance of anisotropy in the physics of dendrites, the dynamics of the protrusion tips in Fig. 8 is probably questionable. In this respect, the variation of Δ_L with V that is found for $V > 0.9375$ cm/s may be over or under estimated. Nevertheless, the finding of the transition towards the protruded state represented by the jump in Δ_L seems to be robust. This statement is underpinned by an additional simulation with $\delta_\sigma = 2\%$ and 4% anisotropy for, respectively, the α-liquid and β-liquid surface tensions, and $\delta_\mu = 10\%$ and 20% for the kinetic coefficient. The orientation-dependent surface tension σ then reads $\sigma(\theta, \varphi) = \sigma_0[1 + \delta_\sigma\{\cos^4\theta + \sin^4\theta(1 - 2\sin^2\varphi\cos^2\varphi)\}]$, and the same formula holds when replacing $\sigma(\theta, \varphi)$ by $\mu(\theta, \varphi)$, σ_0 by μ_0, and δ_σ by δ_μ. Here we assume that the (100) cubic crystalline axis is aligned with the growth axis (the thermal gradient). θ and φ are the usual angles in the spherical coordinate system, i.e., θ is the angle between the normal to the interface and the growth axis, and φ is the angle between one of the remaining cubic axis (010) or (001) and the projection of the normal vector onto the plane perpendicular to the growth axis. Supporting the results for isotropic properties, the simulation also shows protruded states (see movie 2 in the Supplemental Material [42]). We find the latter at $V = 0.79$ cm/s, which is below the transition velocity in the isotropic case that lies between 0.8125 and 0.9375 cm/s, see Fig. 5. This is in line with the fact that the anisotropy of interfacial properties favors the dendritic solution.

Let us now comment on the dynamics of the protrusion in the isotropic case. Near the threshold for its appearance, the protrusion develops and fades away with a relatively small extension in the growth direction, and as can be seen in Fig. 7, it mainly consists of a flat α-liquid interface perpendicular to the growth direction. This flat front dynamics may be described by the driving force Δ_α, which is already close to 0.5 at $V = 1$ cm/s. Δ_α being smaller than unity, the flat front slows down in time (in principle with a velocity that evolves as $1/\sqrt{t}$), and the protrusion vanishes. The development of the protrusion may in principle be understood in terms of a Mullins-Sekerka instability [43], inhibited when Δ_α/l_D is much smaller than Δ_L/λ [see the discussion following Eq. (4)] and able to proceed when they are of the same order. Indeed, for the protrusion to develop, capillary effect should be overcome, and we may thus interpret the splitting of the protrusion tip observed in Fig. 8 as a manifestation of the decrease of the Mullins-Sekerka critical length when the growth velocity increases. Further work is required to understand the dynamics of the protrusion in the anisotropic case.

Let us comment also on the observed increase, when comparing Figs. 7 and 8, of the extension in the growth direction of the protrusion when the velocity increases, i.e., when Δ_L and Δ_α increase. This tendency may be understood using the following theoretical arguments. Since distinct growth modes in general exhibit different power-law relations between their characteristic length scales, velocity, and undercooling, a *concomitant* growth of the corresponding structures at comparable temperatures and velocities is hardly achieved in the WOE regime. In contrast, when the undercooling for the different growth modes become of order unity, as here Δ_L and Δ_α for $V > 0.9375$ cm/s, the different characteristic length scales collapse, with Peclet numbers becoming of order unity (as for example for the cellularlike growth described in Ref. [29], and the coupled growth described above), and the growth temperatures and velocities of the different structures may be close to each other, allowing their concomitant growth. The protruded state may thus be interpreted as the manifestation of the SOE regime. In addition, the concomitant growth yielding the protruded state illustrates the transition between coupled growth at low velocities and single-phase growth at large velocities. The difference of temperature between the protrusion's tip and the eutectic front thus naturally

increases when the growth velocity increases, as observed from Figs. 7 and 8.

We will finally comment on the thermal conditions that were used in our simulations. We have selected values for the cooling rate and the thermal gradient that are in the range of typical experimental conditions for L-PBF [39]. In the simulations, the cooling rate has been varied, while the thermal gradient was kept fixed. While the value of the thermal gradient is usually not key to the understanding of the eutectic coupled growth, it may however have an influence on the development of the protruded state, since the concomitant growth results from the existence of two solutions having close but different growth temperatures. Some future work may thus focus on investigating the effect of the thermal gradient. In particular, how the thermal gradient influences the interval of growth velocities for which concomitant growth is observed needs to be studied.

C. Experiments

The simulation results and the discussion above are supported by experimental results from LPBF for a Al-8 wt. % Ni alloy. Samples have been produced with a 150 °C preheated building platform, at a 10 cm/s laser scanning speed and a 230 W laser power. Each powder layer was 50 μm in height and the hatch distance between different tracks was 135 μm. After being cut, the sample was analyzed under a scanning electron microscope (SEM) after a vibration polishing of the surface. In Fig. 9(a) the solidification microstructure found in the vicinity of the bottom of a melt pool is presented. One identifies the so-called interlayer boundary (ILB), i.e., the region where the material has experienced a vanishing cooling rate at the very bottom of the melt pool. As a result of the time dependent thermal field during the LPBF process, the velocity at which the alloy has solidified increases with the distance to the ILB, resulting in the transition from eutectic coupled growth to single-phase α dendritic growth, as observed. Focusing on the transition region in Fig. 9(b), we see in the lower left corner homogeneously gray regions corresponding to coupled growth, and separated by bright grain boundaries. On the other hand, in the upper right corner a contrast pattern corresponding to α dendritic growth is observed. From the lower left corner to the upper right one, the transition takes place through the appearance of isolated or multiple α cells. Although the transition is quite abrupt, the density of such α cells and the number of cells within a multiplet increase progressively. Finally, a larger magnification of the dashed rectangle is presented in Fig. 9(c), where the eutectic structure surrounding the α multiplets is clearly visible. These experimental results are in full agreement with the phenomenology revealed by the phase field simulations, i.e., the α cells that we observe in the experiment correspond to the cylinder in which β fibers are absent (see description of Fig. 7). Moreover, the characteristic length scales evidenced experimentally, i.e., eutectic spacing and width of the α cells, are in good agreement with the simulations.

Let us comment on the justification of this qualitative comparison between the simulations and the experiment. In each simulation the thermal gradient and the growth velocity are fixed, and the latter changes from one simulation to the other. The question is whether the microstructure observed experimentally in the neighborhood of the transition region corresponds to a succession of quasi-steady-states at different velocities and, at least not significantly varying, thermal gradient. Thus, we want to show that the timescale for the establishment of a quasi-steady-state solidification is much smaller than the characteristic timescale for the evolution of

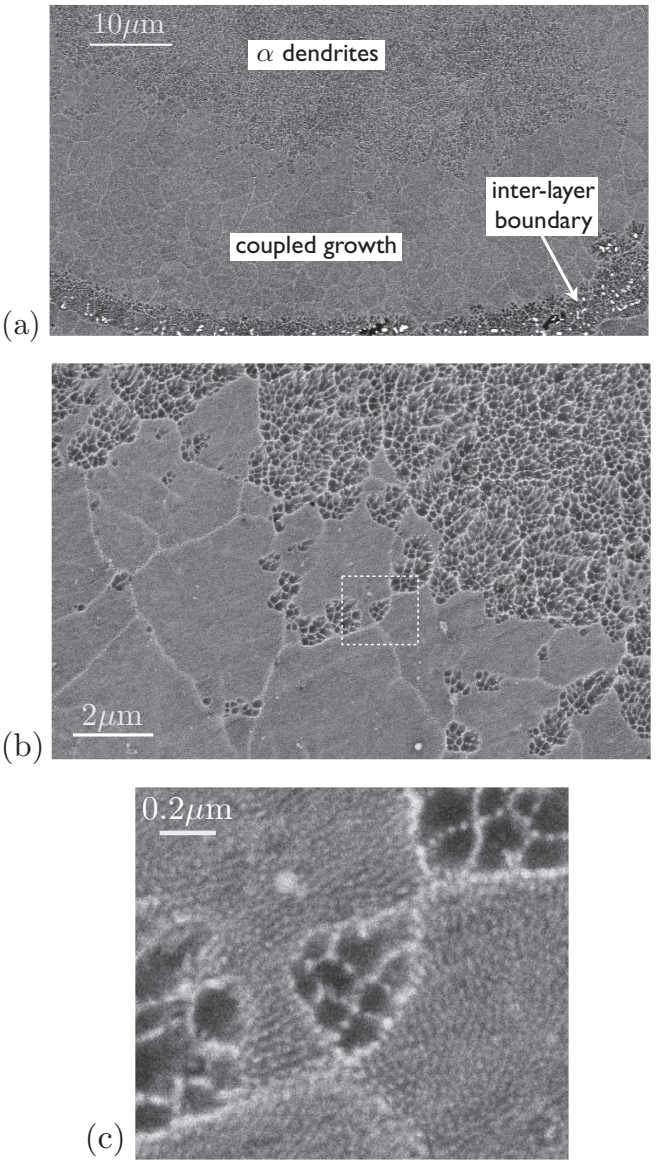

FIG. 9. SEM image of a Al-8 wt. % Ni alloy, that is LPBF processed with a laser scanning speed 10 cm/s (see text for more details). The building direction points out of the plane of the image. In (a) we present the neighborhood of an interlayer boundary (ILB). As the solidification velocity increases with the distance from the ILB, one first observes a region where eutectic coupled growth has taken place and then a region where α dendritic growth occurred. In (b), a closeup is shown on the transition region between coupled growth and dendritic growth. We see isolated or multiple α cells arising progressively as growth velocity increases from the lower left corner to the upper right one. In (c), the region in the dashed rectangle is shown and we see groups of α cells surrounded by the eutectic coupled growth structure.

the solidification velocity. In other words, the relative variation of solidification velocity during the time needed for the establishment of steady state should be negligible. As can be seen in Fig. 9, the radius of curvature of the ILB, which is on the order of the characteristic length scale of the melt pool (in our case the melt pool presents a single characteristic length scale since we are neither in a deep keyhole regime nor in a conduction regime with an elongated melt pool in the scanning direction), is much larger than any other length scale of relevance. These other length scales are the width of the coupled growth or concomitant growth region, the thermal length, which is for a thermal gradient 10^5 K/cm on the order of 10 μm, and the diffusion length, which is smaller than a micrometer for solidification velocities on the order of a tenth of the scanning speed as assumed in our simulations. Since the ILB locates a position where the thermal gradient is finite and the growth velocity vanishes, one may indeed assume that the solidification conditions for the microstructure presented in Fig. 9 correspond to a thermal gradient directed perpendicular to the ILB and having a magnitude that does not significantly vary, and a growth velocity that increases with the distance y to the ILB on the micrograph. For simplicity we assume that the melt pool is an axisymmetric paraboloid around the origin of our system of coordinates. We define x as the scanning direction, y as the built direction, and z as the third direction. The origin moves with the scanning velocity V_S along the x direction, and we focus on the symmetry plane $z = 0$. Then the shape of the melt pool can be written as $y \sim x^2/\rho$, with ρ on the order of the radius of curvature of the ILB. The radius ρ is large compared to the microstructure length scales, and we shall use a small slope approximation, i.e., $y, x \ll \rho$. While the laser moves with velocity V_S, the material solidifies with a growth velocity $V \sim V_S(dy/dx) \sim V_S(x/\rho)$ in the rear of the moving melt pool, at a position x that increases with time t as $x = V_S t$. The time derivative of the growth velocity V is thus $dV/dt \sim V_S^2/\rho$. Moreover, we may assume that the characteristic timescale for the establishment of the steady state is $t_{st} \sim l_D/V$, i.e., that the growth structure covers, with a velocity V, a distance of the order of the diffusion length $l_D \sim D/V$ before reaching steady state. The variation of V during such a timescale $(dV/dt)t_{st}$ is D/y, and should be much smaller than V itself. Thus, the observed microstructure consists of a succession of steady states as long as $y \gg l_D$, which is safely verified in our experiment, with a submicrometer diffusion length. This justifies the comparison between simulations and experiment discussed in this paper.

The phenomenology presented above was also clearly evidenced in the Al-Ce system investigated in Ref. [44]. Al-Ce presents, as Al-Ni, a very asymmetric eutectic phase diagram, and thus should exhibit similar solidification pattern in the SOE regime. We refer in particular, but not exclusively, to the right panel of Fig. 6 in Ref. [44], in which the observation of the concomitant growth of the eutectic structure and of isolated α cells is even clearer than in our experiment.

III. CONCOMITANT GROWTH OF DENDRITES AND DOUBLONS IN SINGLE-PHASE SOLIDIFICATION

The two-dimensional growth of a single fcc phase, i.e., the α phase in the Al-Ni alloy, yields another example of concomitant growth in the SOE regime. As mentioned in the Introduction, growth at typical velocities for LPBF takes place through a cellularlike structure with weakly interacting tips [29]. This yields a disordered array, and in two dimensions an inhomogeneous spacing. Moreover, the tips are growing in the cubic direction of the underlying crystal showing their dendritic nature.

In the theory of dendritic growth for a cubic crystal, there are mainly two kinds of solutions. The first is the classical object with a fourfold symmetry [6]. The other one is called parity-broken dendrite, and in two dimensions is referred to as doublon [8]. Alike the classical dendrite, it assumes an axis of symmetry, but at which a small liquid channel is present. In both cases, the Ivantsov theory holds for the shape of the interface asymptotically far from the tip (which is twofold for the doublon).

For a two-dimensional classical dendrite growing at velocity V_{dendrite} and undercooling Δ_{dendrite}, the scaling relation between these two quantities reads

$$\frac{d_0 V_{\text{dendrite}}}{D} \sim \Delta_{\text{dendrite}}^4 \, \epsilon^{7/4}, \tag{5}$$

with again D the diffusion coefficient in the liquid. As mentioned before, the anisotropy of capillary length (or surface tension) is crucial for the dendritic problem and needs to be accounted for in order to have a solution. One assumes a capillary length that depends on the orientation θ of the interface with respect to the axis of the crystal:

$$d(\theta) = d_0(1 - \epsilon \cos 4\theta). \tag{6}$$

The strength of the anisotropy of capillary length is provided by ϵ, and the corresponding amplitude for the anisotropy of surface tension is $\epsilon/15$.

On the other hand, for a doublon growing at velocity V_{doublon} and undercooling Δ_{doublon}, the scaling relation reads

$$\frac{d_0 V_{\text{doublon}}}{D} \sim \Delta_{\text{doublon}}^9. \tag{7}$$

Moreover, the existence of this solution requires [45]

$$\Delta_{\text{doublon}} > \epsilon^{1/4}. \tag{8}$$

Thus, the competition between the classical dendrite and the doublon crucially depends on the strength of the anisotropy ϵ. While the undercooling of the doublon does not depend on ϵ, the undercooling of the classical dendrite Δ_{dendrite} increases when ϵ decreases. At low anisotropy, the doublon is therefore favorable. For a concomitant growth at $V_{\text{dendrite}} = V_{\text{doublon}}$, the inequality (8) implies

$$\Delta_{\text{doublon}} < \Delta_{\text{dendrite}}^2. \tag{9}$$

Thus, since the latter inequality implies $\Delta_{\text{doublon}} \ll \Delta_{\text{dendrite}}$ when $\Delta_{\text{dendrite}} \ll 1$, we see that a concomitant growth with $\Delta_{\text{dendrite}} \sim \Delta_{\text{doublon}}$ only takes place in the SOE regime, i.e., when Δ_{dendrite} and Δ_{doublon} are of order unity.

Here we illustrate this phenomenon with simulations for which the growth velocity is 12 cm/s and the thermal gradient is 2×10^5 K/cm. While the anisotropy of kinetic coefficient is neglected, we vary the anisotropy of solid/liquid surface tension. The thermal gradient and the axis of the crystal are

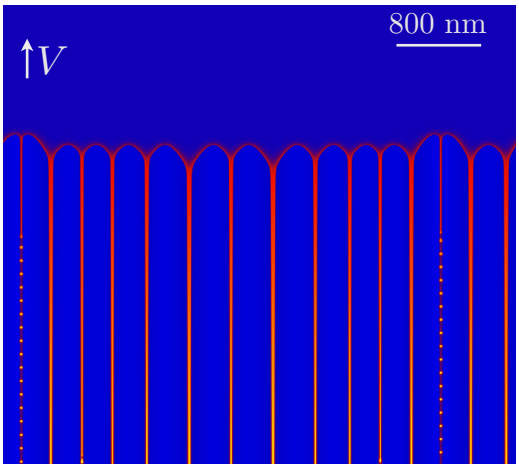

FIG. 10. Two-dimensional cellularlike solidification of the fcc phase, at $V = 12$ cm/s and for a thermal gradient (aligned with the velocity V) equal to 2×10^5 K/cm. We see the concomitant growth of dendrites and doublons, with the latter growing at slightly higher temperature than the former. Here the anisotropy strength (see text) is 0.05.

directed along the velocity V. In Fig. 10 we present the cellularlike array that we obtain for $\epsilon = 0.05$. We distinguish classical dendrites and doublons from the difference in their growth temperature and from the fact that we observe an early decomposition of the liquid channel into droplets at the axis of symmetry of the doublons. Here the anisotropy is rather small. It corresponds to an anisotropy of surface tension of 0.33% (0.05/15). As can be seen in Fig. 11, the difference in growth temperature decreases when ϵ increases. In Fig. 12 we plot the undercoolings Δ_{dendrite} and Δ_{doublon} as a function of ϵ. Owing to the relatively high growth velocity, the undercooling is large. The difference $\Delta_{\text{doublon}} - \Delta_{\text{dendrite}}$ decreases when ϵ increases as inferred from Fig. 11.

We also see that both undercoolings decrease when ϵ increases. On the one hand, this is contradictory to Eq. (7), and on the other hand, the scaling relation in Eq. (5) clearly does not hold in view of Fig. 12. Two arguments may be invoked to explain these discrepancies. First, the scaling laws that are recalled above are derived in the limit of the WOE regime,

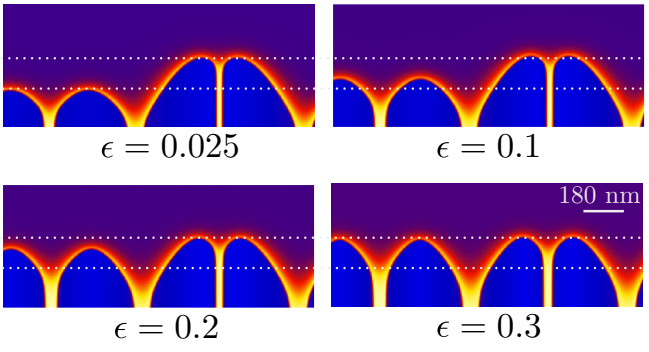

FIG. 11. Closeup on a doublon and its neighboring dendrites, for different values of anisotropy strength ϵ. Small values of ϵ favors the growth of the doublon, i.e., the difference in temperature between the dendrites' tips and the doublon's tip increases when ϵ decreases.

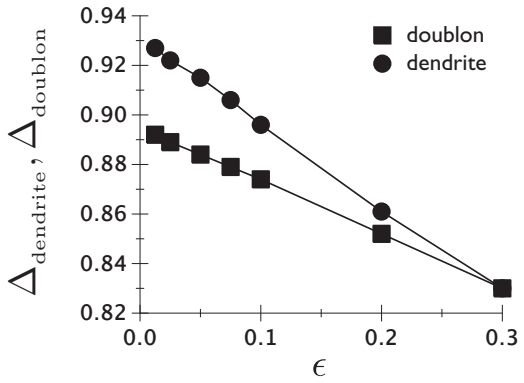

FIG. 12. Undercoolings of the dendrites Δ_{dendrite} and the doublons Δ_{doublon} as a function of the anisotropy strength ϵ.

i.e., for small undercooling, and are thus not expected to hold here in the SOE regime. Second, the scaling laws are derived for isolated objects, while here the microstructure consists of an array of objects interacting via their diffusion field. Note that this interaction, although rather weak, seems sufficient to direct the growth of doublons along the same cubic direction as for the dendritic growth, although an isolated doublon does not have a preferred growth direction.

To summarize, the results of our two-dimensional simulations are in full accordance with the qualitative arguments given above concerning the competition between the dendrite and the doublon, i.e., concerning the fact that less anisotropy favors the doublon. In particular, we have observed that when doublons and dendrites are able to grow at the same velocity and at a comparable undercooling, the anisotropy strength ϵ tunes the difference in temperature of the tips. Moreover, we have shown using theoretical arguments that his concomitant growth is a particularity of the SOE regime of single-phase solidification. Let us finally recall that the phenomenology presented in this section concerns single phase solidification. Thus it corresponds to the scenario where α dendritic growth takes over at larger velocities than the ones investigated in the previous section. As explained above, the protruded state may then be understood as a precursor for this regime.

IV. CONCLUSION

In this article we have studied the development of the strongly out-of-equilibrium (SOE) regime of solidification in the Al-Ni eutectic alloy using phase field simulations. The planar coupled growth of α and β phases destabilizes with increasing growth velocity. The destabilization takes place through a smooth transition towards a chaotic dynamics, followed by a jump in undercooling at larger velocities, corresponding to the development of a protruded state. A concomitant growth of a protrusion of α phase and of the eutectic structure is possible when the undercoolings for eutectic and for single-phase solidification become comparable and of order unity. This concomitant growth is thus a manifestation of the SOE regime. The protrusions leave β free regions in the solid, which has been found also in experiments. We also present two-dimensional simulations of a single-phase solidification structure composed of dendrites and doublons

that provides another example for a concomitant growth under SOE conditions.

ACKNOWLEDGMENTS

We deeply acknowledge the financial support provided by the Deutsche Forschungsgemeinschaft (DFG) in the framework of the Priority Program SPP2122 under Grant No. 409726740. One of the authors (M.D.) gratefully acknowledges funding of the Erlangen Graduate School in Advanced Optical Technologies (SAOT) by the Bavarian State Ministry for Science and Art.

[1] J. S. Langer, Instabilities and pattern formation in crystal growth, Rev. Mod. Phys. **52**, 1 (1980).
[2] G. P. Ivantsov, Temperature field around a spheroidal, cylindrical and acicular crystal growing in a supercooled melt, Dokl. Akad. Nauk SSSR **58**, 567 (1947).
[3] A. Barbieri, D. C. Hong, and J. S. Langer, Velocity selection in the symmetric model of dendritic crystal growth, Phys. Rev. A **35**, 1802 (1987).
[4] Y. Saito, G. Goldbeck-Wood, and H. Müller-Krumbhaar, Numerical simulation of dendritic growth, Phys. Rev. A **38**, 2148 (1988).
[5] E. A. Brener and V. I. Mel'nikov, Pattern selection in two-dimensional dendritic growth, Adv. Phys. **40**, 53 (1991).
[6] E. A. Brener, Needle-Crystal Solution in Three-Dimensional Dendritic Growth, Phys. Rev. Lett. **71**, 3653 (1993).
[7] S. Akamatsu, G. Faivre, and T. Ihle, Symmetry-broken double finger and seaweed patterns in thin-film directional solidification of a nonfaceted cubic crystal, Phys. Rev. E **51**, 4751 (1995).
[8] M. Ben Amar and E. Brener, Parity-Broken Dendrites, Phys. Rev. Lett. **75**, 561 (1995).
[9] K. A. Jackson and J. D. Hunt, Lamellar and rod eutectic growth, Trans. Metal. Soc. AIME **236**, 843 (1966).
[10] M. Ginibre, S. Akamatsu, and G. Faivre, Experimental determination of the stability diagram of a lamellar eutectic growth front, Phys. Rev. E **56**, 780 (1997).
[11] A. Karma and A. Sarkissian, Morphological instabilities of lamellar eutectics, Metal. Mater. Trans. A **27**, 635 (1996).
[12] K. Kassner and C. Misbah, Growth of lamellar eutectic structures: The axisymmetric state, Phys. Rev. A **44**, 6513 (1991).
[13] G. Faivre and J. Mergy, Tilt bifurcation and dynamical selection by tilt domains in thin-film lamellar eutectic growth: Experimental evidence of a tilt bifurcation, Phys. Rev. A **45**, 7320 (1992).
[14] K. Kassner, C. Misbah, and R. Baumann, Eutectic dynamics: a host of new states, Phys. Rev. E **51**, R2751 (1995).
[15] S. Akamatsu, S. Bottin-Rousseau, and G. Fauvre, Experimental Evidence for a Zigzag Bifurcation in Bulk Lamellar Eutectic Growth, Phys. Rev. Lett. **93**, 175701 (2004).
[16] S. Akamatsu and G. Faivre, Traveling waves, two-phase fingers, and eutectic colonies in thin-sample directional solidification of a ternary eutectic alloy, Phys. Rev. E **61**, 3757 (2000).
[17] S. Akamatsu, M. Perrut, S. Bottin-Rousseau, and G. Faivre, Spiral Two-Phase Dendrites, Phys. Rev. Lett. **104**, 056101 (2010).
[18] G. Boussinot, C. Hüter, and E. A. Brener, Growth of a two-phase finger in eutectics systems, Phys. Rev. E **83**, 020601(R) (2011).
[19] A. Karma and W.-J. Rappel, Quantitative phase-field modeling of dendritic growth in two and three dimensions, Phys. Rev. E **57**, 4323 (1998).
[20] T. Takaki, S. Sakane, M. Ohno, Y. Shibuta, T. Aoki, and C.-A. Gandin, Competitive grain growth during directional solidification of a polycrystalline binary alloy: Three-dimensional large-scale phase-field study, Materialia **1**, 104 (2018).
[21] A. Parisi and M. Plapp, Defects and multistability in eutectic solidification pattern, Europhys. Lett. **90**, 26010 (2010).
[22] A. Parisi and M. Plapp, Stability of lamellar eutectic growth, Acta Mater. **56**, 1348 (2008).
[23] T. Pusztai, L. Rátkai, A. Szállás, and L. Gránásy, Spiraling eutectic dendrites, Phys. Rev. E **87**, 032401 (2013).
[24] K. Wang, G. Boussinot, C. Hüter, E. A. Brener, and R. Spatschek, Modeling of dendritic growth using a quantitative nondiagonal phase field model, Phys. Rev. Materials **4**, 033802 (2020).
[25] E. A. Brener and G. Boussinot, Kinetic cross coupling between nonconserved and conserved fields in phase field models, Phys. Rev. E **86**, 060601(R) (2012).
[26] O. Funke, G. Phanikumar, P. K. Galenko, L. Chernova, S. Reutzel, M. Kolbe, and D. M. Herlach, Dendritic growth velocity in levitated undercooled nickel melts, J. Cryst. Growth **297**, 211 (2006).
[27] P. K. Galenko, S. Reutzel, D. M. Herlach, S. G. Fries, I. Steinbach, and M. Apel, Dendritic solidification in undercooled Ni-Zr-Al melts: Experiments and modeling, Acta Mater. **57**, 6166 (2009).
[28] H. Müller-Krumbhaar, W. Kurz, and E. Brener, *Phase Transformations in Materials*, edited by G. Kostorz (Wiley-VCH, Berlin, 2001).
[29] G. Boussinot, M. Apel, J. Zielinski, U. Hecht, and J.-H. Schleifenbaum, Strongly Out-of-Equilibrium Columnar Solidification During Laser Powder-Bed Fusion in Additive Manufacturing, Phys. Rev. Appl. **11**, 014025 (2019).
[30] L. Ratke and J. Alkemper, Ordering of the fibrous eutectic microstructure of Al-Al_3Ni due to accelerated solidification conditions, Acta Mater. **48**, 1939 (2000).
[31] M. Apel, B. Boettger, H.-J. Diepers, and I. Steinbach, 2D and 3D phase-field simulations of lamella and fibrous eutectic growth, J. Cryst. Growth **237-239**, 154 (2002).
[32] W. Kurz and D. J. Fisher, Dendrite growth in eutectic alloys: The coupled zone, Inte. Metals Rev. **24**, 177 (1979).
[33] G. Boussinot, M. Döring, S. Hemes, O. Stryzhyboroda, M. Apel, and M. Schmidt, Laser powder bed fusion of eutectic Al-Ni alloys: Experimental and phase-field studies, Mater. Design **198**, 109299 (2021).
[34] M. Apel, G. Boussinot, M. Döring, and M. Schmidt, Eutectic solidification in Al-Ni for L-PBF conditions: A phase-field study, Procedia CIRP **94**, 64 (2020).
[35] R. S. Barclay, H. W. Kerr, and P. Niessen, Off-eutectic composite solidification and properties in Al-Ni and Al-Co alloys, J. Mater. Sci. **6**, 1168 (1971).
[36] www.micress.de (version 6.4).

[37] J. Eiken, B. Böttger, and I. Steinbach, Multiphase-field approach for multicomponent alloys with extrapolation scheme for numerical application, Phys. Rev. E **73**, 066122 (2006).

[38] B. Böttger, M. Apel, M. Budnitzki, J. Eiken, G. Laschet, and B. Zhou, Calphad coupled phase-field model with mechano-chemical contributions and its application to rafting of γ' in CMSX-4, Comput. Mater. Sci. **184**, 109909 (2020).

[39] T. Keller, G. Lindwall, S. Ghosh, L. Ma, B. M. Lane, F. Zhang, U. R. Kattner, E. A. Lass, J. C. Heigel, Y. Idell, M. E. Williams, A. J. Allen, J. E. Guyer, and L. E. Levine, Application of finite element, phase-field and CALPHAD-based methods to additive manufacturing of Ni-based superalloys, Acta Mater. **139**, 244 (2017).

[40] S. Akamatsu, G. Faivre, and S. Moulinet, The formation of lamellar-eutectic grains in thin samples, Metal. Mater. Trans. A **32**, 2039 (2001).

[41] R. Folch and M. Plapp, Phase-field modeling of eutectic solidification: From oscillations to invasion, in *Interface and Transport Dynamics*, edited by H. Emmerich, B. Nestler, and M. Schreckenberg, Lecture Notes in Computational Science and Engineering, Vol. 32 (Springer, Berlin, 2003).

[42] See Supplemental Material at http://link.aps.org/supplemental/10.1103/PhysRevMaterials.6.043405 for visualizing the protrusion evolution under isotropic (movie 1) and anisotropic (movie 2) interfacial properties.

[43] W. W. Mullins and R. F. Sekerka, Stability of a planar interface during solidification of a dilute binary alloy, J. Appl. Phys. **35**, 444 (1964).

[44] A. Plotkowski, O. Rios, N. Sridharan, Z. Sims, K. Unocic, R. T. Ott, R. R. Dehoff, and S. S. Babu, Evaluation of an Al-Ce alloy for laser additive manufacturing, Acta Mater. **126**, 507 (2017).

[45] E. Brener, H. Müller-Krumbhaar, and D. Temkin, Structure formation and the morphology diagram of possible structures in two-dimensional diffusional growth, Phys. Rev. E **54**, 2714 (1996).